Multifunctional Arm for Telerobotic Wind Turbine Blade Repair

Rasoul Sadeghian and Sina Sareh, *Member IEEE*

***Abstract*—Within the Multi-Platform Inspection, Maintenance and Repair in Extreme Environments (MIMRee) project, a lightweight and multifunctional robotic repair arm is created for wind turbine blades. The design features a toolbox at the base of the arm housing multiple end-effector tools and an autonomous end-effector tool-changer. The arm communicates commands and data via internet with a bespoke user interface enabling human-in-the-loop operation and overriding of autonomous repair actions. This paper outlines our approach in design, development, testing and control of the robotic repair system. The functionalities of the arm include cleaning, sanding, and filler material deposition and forming, each using a bespoke end-effector tool closely replicating the relevant manual repair process. The experimental results confirm the effectiveness of our approach indicating a maximum end-effector position error of 3 mm, a maximum tool switching time of 8 seconds, and a maximum arm's weight of 1.8 kg. This presents around 84% weight reduction compared with existing technologies used for the same purpose. Our standalone design enables modular integration into a wide range of mobile platform types used in industrial operations.**

I. Introduction

People who need to work at height, underground or in hazardous locations have higher health risks due to falling, exposures to toxic chemicals and radiation or other aspects of their work. The maintenance and repair of wind turbine blades at extreme offshore environments presents one of the most hazardous work locations.

Offshore wind farms, a group of wind turbines in bodies of water used to produce electricity, are a rapidly maturing renewable energy resource that is set to play an important role in future energy systems. In order to increase the wind farm efficiency, blades, currently around 80m long, will get progressively larger [1]. The blades are typically constructed from composite materials and can be damaged by cracking, delamination and erosion during the service [2]. Hence, regular inspection and repair of composite wind turbine blades is essential. The inspection and repair of offshore wind turbines blades are typically performed by rope access technicians who need to deal with challenging offshore conditions at height including lightning strikes, squalls and gales, as well as wave heights that make the transfer from vessels to the wind turbine platforms highly dangerous [3].

R. Sadeghian and S. Sareh are with RCA Robotics Laboratory, Royal College of Art, London, UK (email for corresponding author: sina.sareh@rca.ac.uk).

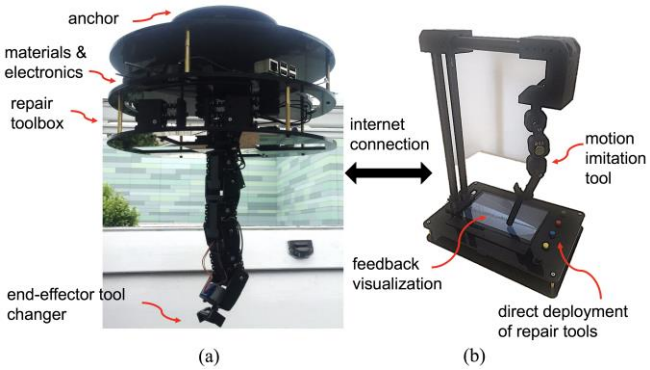

Figure 1. Autonomous repair arm: (a) multifunctional and tetherless robot arm, and (b) bespoke user interface for human-in-the-loop operation.

A number of technology companies have developed robotic systems for wind turbine inspection and maintenance. Prominent examples with a focus on blade inspection and repair include Sandia National Labs, USA, and Rope Robotics Ltd, Denmark. While the current publication [4] on Sandia's robot indicates a focus on the mobility and imaging platforms, the BR-8 robot [5] by Rope Robotics Ltd is integrated with a standard robot arm (UR3) produced by Universal Robotics, Ltd, and can travel along the length of a turbine blade using pre-laid ropes. However, the ropes should be initially installed into the wind turbine structure by human workers. The choice of a pre-laid rope-based mobility platform could be due to the high load-ability needed to safely carry the UR3 arm, which weighs around 11kg excluding any repair tools.

Within the Multi-Platform Inspection, Maintenance and Repair in Extreme Environments (MIMRee) project [6], we propose a lightweight multifunctional robotic repair arm that is designed specifically for applications in mobile repair. The arm is amenable for modular integration into a wide range of robot mobility platform typologies, Fig. 1.

The contributions of this paper include the development of: (1) an autonomous repair arm integrated with a custom end-effector tool-changer that enables autonomous switch between multiple repair tools (multifunctional), (2) bespoke repair tools for cleaning, sanding, filling and forming of blade damages closely replicating the counterpart manual processes employed in the repair of wind turbine blades, (3) a bespoke user interface (UI) that enables the imitation of technician's hand motion and provides visual and collision feedback to the operator, and (4) an image processing algorithm that enables autonomous evaluation of the repair work during the repair process. In addition, we have addressed a number of control

challenges improving the end-effector tool changing process, filler material deposition, and repair tools' activation trigger.

This paper is organized as follows: Section II explains the erosion issue at the leading-edge (LE) of composite wind turbine blades and relevant manual repair processes and requirements. Section III describes the electromechanical design and fabrication of the arm, repair system and the UI. In Section IV the control issues of the arm and repair tools are described and effective solutions to the issues are proposed. Section V describes the conclusions of this research and potential future developments.

II. Application Context and Requirements

A. Leading Edge Erosion in Composite Turbine Blades

While the generator, tower and hub of wind turbines are typically manufactured from metals, composite materials are widely used in the construction of blades and nacelles. The complex loading applied to the blade as well as the environmental effects, such as rain droplets, can result in a wide range of damages to wind turbine blades including, and not limited to, Leading Edge (LE) Erosion, Fig. 2a. The LE Erosion increases the extent of transitional flow over the blade and reduces its aerodynamic properties. This research has devoted a particular focus to the development of repair mechanisms for LE Erosion [2,3].

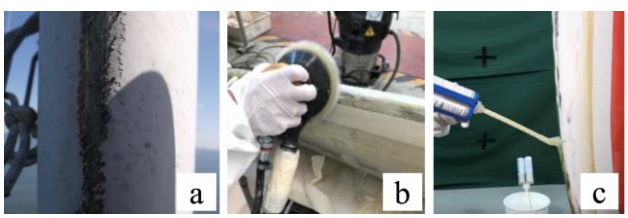

Figure 2. (a) LE Erosion in a composite wind turbine blade [reproduced with permission from ORE Catapult], (b) sanding, and (c) deposition of the filler materials on the blade [b,c are reproduced with permission from Teknos [7]].

B. Materials and Processes for Blades' Manual Repair

In this study, we chose the elastomer-based coating technology TEKNOBLADE REPAIR 9000™, Teknos Ltd., Finland as the blade repair material. This product has the capability of repairing damaged edges in one single coating, which can simplify the repair process. With reference to the material documentations [7], the manual repair process for LE Erosion problem can be summarised as follows: (1) preparation of the surface with sandpaper, (2) cleaning of the surface, (3) applying the filler materials and forming it to retrieve the original blade edge geometry Figs. 2b, c.

C. Usability Requirements for the Manipulation and Repair System and Respective Technical Challenges

The arm's design aimed at satisfying the multi-platform mobility and functionality requirements of the MIMRee project; the arm should be integrated into a crawling robot platform. The crawling robot integrated with the repair arm should be displaced to the wind turbine blade using an unmanned aerial vehicle (UAV). While at the blade, the arm should be able to carry out multiple tasks to eliminate the need for human presence at the repair site. Hence, the criteria can be summarised as follows: (1) multi-functionality: the ability to switch between multiple repair tasks autonomously and within the overall time constraint of repair material reaction and curing process (6 mins), (2) light-weighting and compactness: the repair arm should meet the payload requirements of the UAV and should fit within the allocated space on the crawling robot. The allocated weight for the arm is 2 kg and the allocated space on the crawling robot is a cylindrical space within a radius of 14 cm and a height of 33 cm, (3) autonomy: the ability for on-board sensing, decision making and execution, particularly for the tasks that can be negatively impacted by network delay when off-board processors used, (4) human-in-the-loop operation and overriding of commands: while the repair mission can be designed to be autonomous in part, keeping human in the loop via a remote UI is not only essential for safety reasons, but also can enable direct incorporation of technician's tacit knowledge into the process, and (5) manipulability: the ability of the arm's end-effectors to reach to different required positions within the defined region for repair. Hence, the technical challenge to satisfy the above requirements can be summarized as: (1) achieving a consistent electromechanical design satisfying the application criteria, e.g. in our system weight and size restrictions, (2) developing relevant algorithms for defect defection on the surface, planning for required motion of the arm enabling the repair, ensuring consistent release of the repair material, e.g. preventing material clogging, and evaluating the repair quality.

III. System Design

The presented system consists of three main parts, a manipulation arm, four repair tools, and a UI that can enable imitation of the user's hand (stylus) motion by the arm, as well as the provision of sensory feedback.

A. Design of the Manipulation Arm

Taking into account the usability requirements for the arm discussed in Section 2.1, the arm has been designed with two main parts: (1) a control, communication, materials and tooling (CMT) unit, and (2) a serial 5R motor assembly, described in the following:

(1) CMT unit: the control, communication, material and tooling unit, accommodated within a custom three-layer cluster case (see Fig. 3a) structured as follows: a top layer (L_A) that is integrated with the mounting mechanism for arm attachment, a middle layer (L_{CM}) housing electronics for communication & control and material supply and dispensing mechanisms, and a base layer (L_T) which accommodates up to four end-effector tools (toolbox layer). As shown in the Fig. 3a, L_{CM} houses the control boards; an Arduino UNO and a Raspberry Pi 3 B+ as well as the material dispensing mechanisms for the repair system, explained in the next section. The L_T layer accommodates four retractable clamping mechanisms to hold the end-effector repair tools while they are not in use. The mechanism for clamping uses a set of 3D printed rods, compression springs and mounting structures and requires no electronics (Fig. 3a). As energy management is a crucial design component in tele-robotic systems, the use of a passive clamping mechanism is highly advantageous.

(2) Serial 5R motor assembly: the 5R assembly, presented

in Fig. 3b, uses four Dynamixel AX−18A servo motors (Robotis, USA) and one 12V 28BYJ−48 stepper motor for the actuation of the assembly joints. The servo motors are connected to each other based on a daisy-chain connection; note that a daisy chain is a wiring scheme in which multiple devices are wired together in sequence. This enables reducing the number of wires. Moving away from the base of the arm motors are numbered from 1 to 5. While the servo motor 1 enables 300 degrees of rotation of the assembly, the rest of three servos are in charge of in-plane bending. Located at the tip of the assembly is the male part of the end-effector tool-changer which uses the stepper motor. The tool-changer mechanism enables switching between multiple end-effectors stored within the L_T layer. Note that a variable resistor is used to find the position of the fifth link, Fig. 3c. Moreover, all end-effectors are integrated with a U-shape latching mechanism, which is the female part of the tool-changer, as shown in Fig. 4a, d, e. All 3D-printed parts of the 5R assembly are fabricated using Onyx material via a Mark Two 3D printer (Markforged, USA). The material allows up to 44% reduction in the weight of the assembly when compared with widely used Aluminum 6061 as a typical fabrication material.

Note that the choice of motors was decided based on the amount of torque needed to manipulate various end-effector repair tools. Our heaviest repair tool, explained in the next section, weighs 67 grams. It is clear that the highest loading occurs on servo motor 2 when it bends at 90 degrees. The relevant torque calculated via ($\tau = r\,F \sin\theta$) is equal to 0.882 N.m, where r, F, θ represent torque, the distance from the center of the rotational-axis of the motor 2 to the tip of the end-effector, the magnitude of the force applied, and the angle between the position and force vectors, respectively. In order to increase the reliability of the system we added 30% of its value to the calculated torque as a design safety factor, reaching a toque requirement of approximately 1.15 Nm for motor 2 which is under the highest load, Fig. 3e.

In this study, we have used the forward and inverse kinematics of the 5R assembly explained in [10]. In order to find the end-effector's accessible areas, the arm's workspace is calculated using the Monte-Carlo method explained in [11] and forward kinematics [10], as shown in Fig. 3f.

B. Design of the repair system

(1) Cleaning module: *a*s summarized in the Table 1, the repair module for cleaning will be in charge of the removal of loose materials on the surface and wet cleaning. In order to address these requirements, the module is designed in two parts to minimize the loading on the 5R assembly: (1) controllable dispenser, using a 12 V DC encoder gear motor running at 100 revolutions per minute (rpm), to automatically release the cleaning liquid. This part is installed within the L_{CM} layer of the arm's CMT unit, and (2) a rotary cleaning end-effector mountable at the tip of the 5R assembly comprised of a cleaning drum and a casing structure. The two parts are linked via a 4mm OD flexible tubing. The drum of the cleaning module's end-effector is fabricated from three layers of materials that differ in mechanical stiffness. This stiffness-gradient architecture of the drum uses a rigid shaft made of PLA materials at the center covered by two layers of soft and flexible materials including a 3mm-thin layer of Mold MAX NV14 tin-catalyzed silicone rubber (Smooth-on Inc., USA) in the middle, and a layer of microfiber fabric which covers its external surface to enable cleaning (see Fig. 4d). While the rigid PLA shaft provides stiffness to maintain the geometrical form of the drum as part of the cleaning end-effector assembly, the silicone rubber and microfiber layers supply sufficient flexibility to enable conformation to the curved shape or damaged texture of the blade to clean it more effectively. The drum is integrated into the casing structure via two metal ball-bearings. It should be mentioned that the mechanical design of the drum and the assembly constraints with its casing structure allow a maximum deformation curvature of $\beta=43^{\circ}$ on the drum's external surface, as shown in Fig. 4b, c. A 12 V DC encoder gear motor running at 300 rpm is in charge of moving the drum via a 3D-printed gear. The position information provided by the two motor encoders, within the cleaning liquid dispenser module and the cleaning end-effector, enables controlling the release-rate of the cleaning liquid to the microfiber material as well as the drum rotational speed to carry out an effective cleaning task.

(2) Sanding end-effector: the structure of the sanding end-effector is very similar to the cleaning end-effector. However, the sanding drum is fabricated purely from rigid PLA materials and the drum's external surface is covered by a layer of sandpaper. We have fabricated two sanding drums with grits of 60 and 80, as advised by TEKNOBLADE REPAIR 9000-10 material application guidelines (see Fig. 4a).

(3) Filler deposition module: the filler deposition module should dispense and mix the two material parts of the TEKNOBLADE REPAIR 9000-10 kit and apply it to the damaged area, after completion of the sanding and cleaning tasks. In order to restore the geometrical shape of the blade at the leading edge, we have developed a bespoke combination of a dynamic mixer with a curved dual-function slit nozzle integrated spatula (Teknos, Finland) for filling and forming of the blade eroded regions. This module is comprised of three parts linked via a 4mm OD tubing including a two-part material dispenser driven by a 12 V DC encoder gear motor running at 250 rpm, located within the L_{CM} layer. The two material outlets of the dispenser are merged to a single tubing and fed into a dynamic mixer (3M, USA), Fig.9a. Subsequently, the mixed material is moved to a spatula for application to the blade, Fig. 4e. Note that the TEKNOBLADE REPAIR 9000-10 is a two-pack, solvent-free elastomeric coating. According to the material's technical datasheet [7], the recommended film thickness of this material (one layer of deposition at time) is 2mm. To ensure this, we integrated the arm with a proximity sensor which comprises of a fiber-optic sensor FS-N11MN, [12], and an optical fiber unit FU-69U (Keyence Co., Japan) located within the electronics and material layer of cluster casing unit to continuously measure the plunger position and provide the position feedback to the Fuzzy-PID controller (Fig. 3d).

The overall weight and height of the arm are 1.8 kg and 31 cm, respectively, which satisfies the requirements for transportation using a UAV, and integration into the crawler.

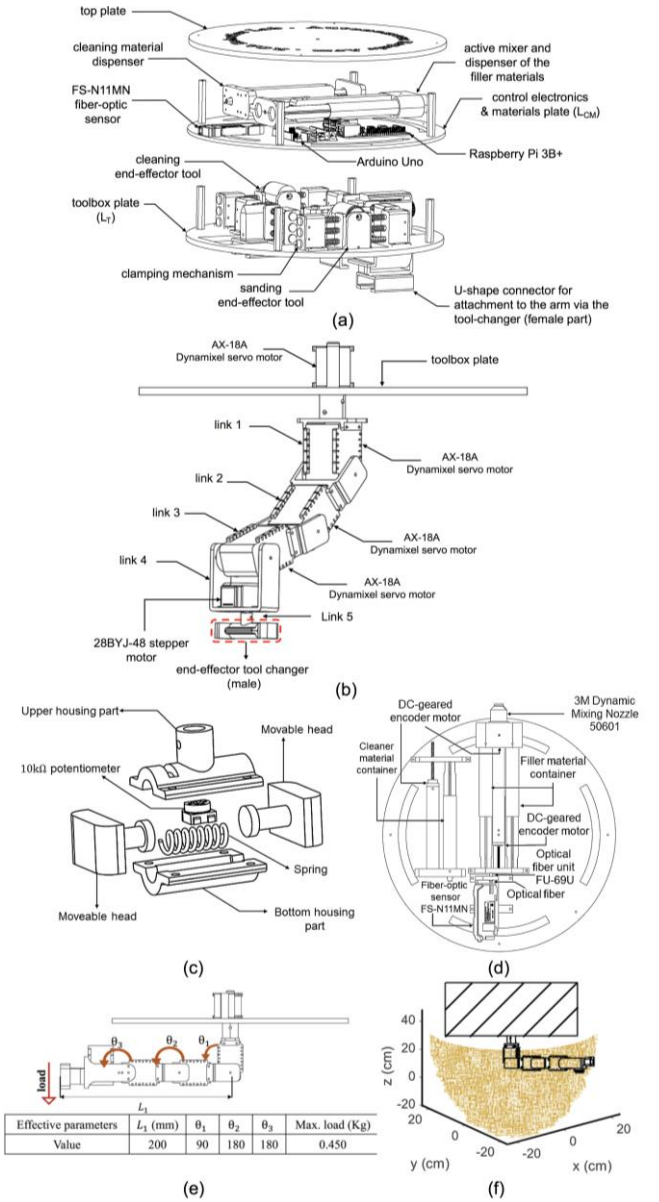

Figure 3. (a) The arm's cluster casing unit comprising of materials, electronics and toolbox layers, (b) the structure of the arm's 5R motor assembly and tool-changer, (c) exploded view of the male part of the tool-changer using a 10 kΩ potentiometer for position encoding, (d) FS-N11MN senor measures the syringe's plunger position, (e) the arm's load tests, and (f) the arm's workspace calculated using the Monte-Carlo method and the arm's forward kinematics.

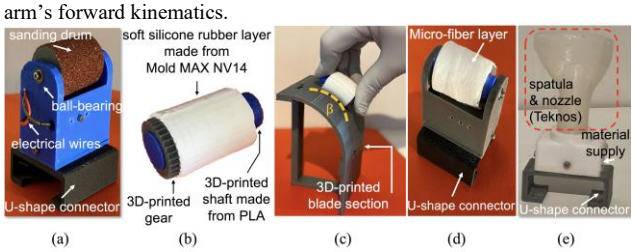

Figure 4. (a) The sanding end-effector integrated with the U-shape connector (female part of the tool-changer) for attachment to the arm, (b) the cleaning drum featuring a stiffness-gradient in its mechanical structure using a rigid core and a 3 mm think middle layer made of soft silicone rubber, (c) the cleaning drum can conform to the curved shape of the blade, (d) the cleaning drum is covered by micro-fiber on its outer surface, and is integrated into end-effector casing, and (e) the filling & forming end-effectors comprised of a curved spatula integrated with an slit nozzle (Teknos, Finland).

C. User Interface

In order to enable human-in-the-loop operation or override of potentially autonomous tasks, a bespoke UI has been developed, Fig. 1b and Fig. 5c.

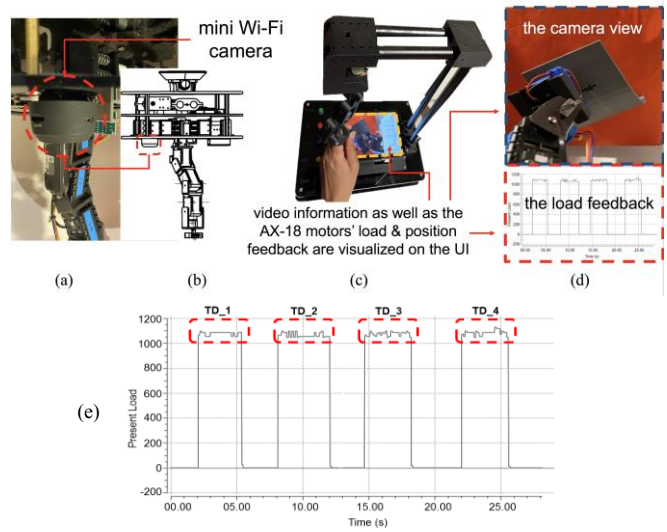

Figure 5. (a,b) the location of the base camera on the arm, (c) video information recorded by the camera and motors' load outputs are visualized on the UI's screen in real-time, (d) the UI's screen, and (e) the load feedback provides an indication of physical interactions between end-effector tools and the blade that can potentially damage the blade, and hence is important to be monitored. TD_1 to TD_4 indicate that the arm's end-effector is dealing with some resistance to move.

The UI is comprised of a multi-segment motion imitation tool, a Raspberry Pi 4, a 7-inch touch screen display, and 5 self-locking latching buttons which enable sending predefined commands to the arm. In between each two segments of the imitation tool, a 10 kΩ potentiometer is integrated on the joint to measure the joint motion. The motion is then mapped and imitated by the 5R assembly of the manipulation arm. In our setting, there are five predefined functions that can be communicated via the UI's function buttons, 'HOME', 'SAND', 'CLEAN', 'FILL' and 'SPATULA'. When the operator presses any button, the motorized joints of 5R assembly will be displaced to position the arm's tip in the relevant predefined location. By pressing the HOME button, the arm moves so that its tip will be located at [0,0,0] position in 3D space. When the operator presses on any of the function buttons the arm moves towards the toolbox layer of the CMT unit and the tool-changer mechanism latches onto the relevant end-effector tool in the toolbox and comes with that end-effector tool to the Home position. Then the operator can continue the repair process with the new end-effector tool. A second press returns the end-effector to the toolbox and the arm to the HOME position. In order to communicate information between the UI and the arm, a method to translate the imitation tool's potentiometers data and key functions was developed that uses Rosbridge Websocket to send /sensor msgs/joy message data types to the arm [8]. Note that ROS is run on Raspberry Pi 4 at both sides.

IV. Control Systems

In our initial tests, three main control challenges were identified which occur during the operation of the arm and the repair system including end-effector tool latching error, tool

activation trigger error, and crack onset point detection error, all of them were of the type "position error". Hence, different strategies for position control were investigated, as follows.

A. End-Effector Tool-Change Control

A main problem in autonomous changing of the end-effector tools is the displacement error making it difficult for the arm to latch onto the repair tool or release it in a predefined toolbox position. Figs 7a, b show the displacement errors occurred during the arm's autonomous latching onto a repair tool as well as releasing it. It can be seen that, the collision with toolbox plate, and lack of ability to reach the repair tool's toolbox positions are the possible sources of displacement error. We applied an adjustable proportional controller to remove the errors, which showed to be sufficient to enable successful tool change (see Fig. 7c).

In order for the end-effector to reach the desired position, clearly, the control error must be close to zero. The position control error of the arm is defined as $e(t) = \varphi_d(t) - \varphi_a(t)$

where, φ_d and φ_a are the desired and actual joint positions, respectively. The proportional gain is adjusted to effectively reduce the control error close to zero during the operating time, t. In Fig. 6, P_d is the desired position, e_{p_1}, ..., e_{p_5} are control errors, C_1, ..., C_5 are controllers, u_1, ..., u_5 are control signals, and θ_1, ..., θ_5 are position feedbacks for joints 1 to 5. In this arrangement, any input to the UI, e.g. via the imitation tool, is mapped using the inverse kinematics model and the calculated angular position is sent to the control unit. Any deviation from the desired calculated path is considered as a control error to be compensated via the controller. Moreover, in the case of autonomous changing of the repair tools, the relevant toolbox position is defined for the arm, and the controller will correct the trajectory if there is any deviation. We performed 10 experiments to measure the ability of the arm in following desired trajectory paths with and without the controller (see Fig. 7c). It was observed that the controller reduced the average error from 36 mm to 7 mm. Table I presents the maximum deviation happened with and without the controller for repair tools with different weights indicating that increasing the weight of the repair tools has a direct effect in increasing the arm's deviation from the desired path.

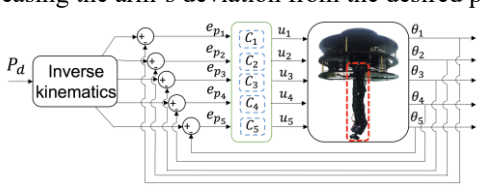

Figure 6. The control diagram for the end-effector tool-changer using the inverse kinematics of the arm.

TABLE I. THE MAXIMUM DEVIATION OCCURRED WITH AND WITHOUT THE CONTROLLER FOR DIFFERENT TOOLS.

Repair tool	W	D_{wc}	D_c
Sanding end-effector	63	1.1	0.2
Cleaning end-effector	67	1.3	0.2
Filling & forming end-effector	45	0.7	0.1

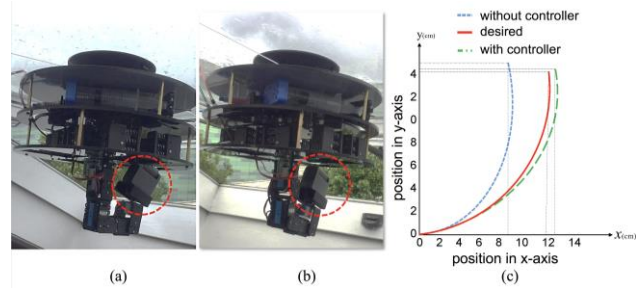

Figure 7. (a) The collision with the toolbox plate and (b) lack of ability to reach the repair tool's toolbox positions are two prominent errors in tool switching, and (c) the performance of the arm in following the desired trajectory for successful tool switching with and without the controller.

B. Filler Material Dispense Control

The accurate control on the release of the filler material is essential for the repair process. The frictional pressure inside a syringe's barrel is a function of the amount of remaining material inside the barrel [13]. As the amount of the material inside the barrel is reduced through dispensing, less force is needed to move the syringe's plunger to dispense the rest of the material. This variation in the driving force requirements leads to displacement errors in plunger motion, and hence inaccuracies in material releasing if an effective control system is not incorporated.

The material dispenser uses a DC encoder gear motor which runs at a constant speed to release the material, as shown in Fig. 8a. The encoder provides information on the syringe's plunger displacement. The ground truth position of the plunger is continuously measured via an FS-N11MN fiber-optic sensor. Note that for the syringe used in this study the plunger should be displaced 3.8 mm for the release of 1ml of material. In order to find a relationship between the amount of material that is released and the amount of motor's angular displacement, an initial calibration test was performed. In this experiment a syringe full of materials (25ml) was completely discharged in 10800 encoder pulses. Hence, the number of pulses that the encoder should count to release a desired amount of material, M_d, can be calculated as,

$$pulse_{release} = \frac{10800 \times M_d}{25} \qquad (1)$$

During the repair process, when the operator inputs a value for the amount of material to be released, the system uses Eq. (1) to compute the required number of angular displacements for the motor shaft and activates the motor accordingly. When the release of material is completed the syringe plunger displacement is measured by the fiber-optic sensor and the amount of released material is calculated based on plunger displacement and compared with counterpart values from the encoder. Any difference between the two values indicates a displacement error. To compensate for the error, a Fuzzy-PID controller is implemented on the dispenser mechanism, where fuzzy logics are used to tune the PID values. Fig. 8b presents the respective control diagram. The design of this controller is detailed in [14], hence we avoid repeating here. Fig. 8c shows the test results for dispensing 5, 10, 15 and 20 ml of the filler material. The actual amounts of the released materials were confirmed with a weighing scale.

C. *End-effector tools' activation trigger control*

The activation of the end-effector tools via sending commands from the UI is influenced by the internet network delay. This delay can negatively impact the execution of repair tasks by causing a position drift; the filling end-effector would start and stop material deposition with a delay causing a lack of material coverage in some areas and waste of material in some other areas. Hence, the activation of the repair tools should be triggered autonomously via an onboard controller as an overridable default specification. According to our experiments, there is a delay between 1 s to 2.7 s in receiving the UI commands by the arm. Considering that the arm moves with a constant speed of 4 rpm and if the shortest amount of teleoperation latency occur, the nozzle will miss the end of the eroded area and stops at a point around 80 mm away, while still releasing the materials, which can produce new issues.

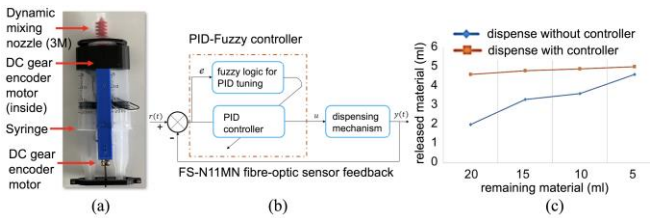

Figure 8. (a) The two-part material dispenser and mixer, (b) the PID-Fuzzy controller diagram, and (c) the experimental results show improvement in material dispensing when the controller is applied.

Algorithm 1: Erosion onset and end point detection by using contours.

```
Input: one video frame;
resize the input frame;
convert the input frame to grayscale (img);
apply the morphological transformation to reduce the img noise;
apply the Canny algorithm to detect the img edges;
using cv2.findContours to get the img's contours;
for contour in contours:
        ac = area of contour;
        if ac > min then:
            draw contour;
    else
        print('there is not any defect.');
```

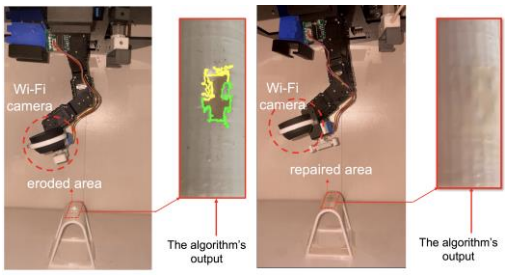

Figure 9. The application of the erosion detection algorithm: (a) The onset and end-point of the detected erosion are indicated with green and yellow, and (b) the algorithm autonomously confirms the completion of repair.

To enable autonomous activation of repair tools triggered by reaching an erosion onset point, and similarly deactivation by meeting the erosion endpoints within the damaged region of the blade, the visual information from two Wi-Fi cameras one installed at the arm's base and one near the arm's end-effector are used. This information is processed onboard of the robotic arm using a custom image processing code developed in Python, Algorithm 1, which initially applies a morphological transformation to reduce the image noise. Then, the cv2.findContours function in the OpenCV library is used for generating contours around the eroded areas. Note that the *ac* variable in the algorithm refers to the area of the contour. The algorithm output is shown in Fig. 9.

D. *Experimental testing*

In order to evaluate the performance of the repair arm a complete process of repairing on the leading edge of a 3D printed section of a turbine blade with a defected area was designed and implemented. The surface of blade was initially scanned to detect the erosion using the detection algorithm. Then the sanding, cleaning, filling and forming tools were applied, Fig. 10. At the end of the repair process the erosion detection algorithm did not detect any erosion and therefore the repair process was completed, similar to Fig. 9b.

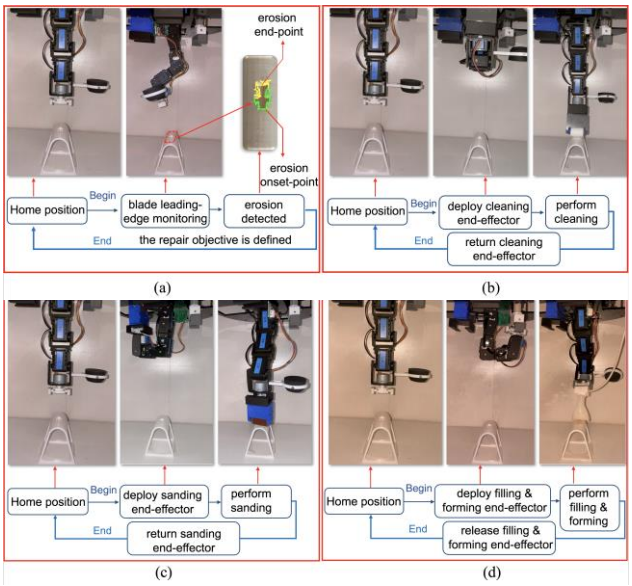

Figure 10. A complete testing of the proposed repair method for blade's LE Erosion: (a) erosion detection and defining the repair objective, (b) cleaning of the area, (c) sanding, (d) filling & forming.

V. Conclusions

A multifunctional robotic arm is developed integrated with multiple repair end-effectors and a bespoke autonomous tool changing mechanism that enables fast switching between different tools. The arm is paired with a custom user interface that acts as a motion imitator for the arm, enabling the incorporation of technicians' tacit knowledge into the robotic repair process. An image processing algorithm is developed that enables autonomous evaluation of the repair work during the repair process. The future research will include the integration of the arm into a mobile robot platform and relevant laboratory and field testing of the integrated system.

Acknowledgment

The work is supported by the Innovate UK (MIMRee project; reference: 104821) and the EPSRC UKRI Fellowship (EP/S001840/1). We would also like to thank Teknos UK Ltd and ORE Catapult for their guidance and support.

References

[1] P.J.H. Volker, AN. Hahmann, J. Badger, HE. Jørgensen,"Prospects for generating electricity by large onshore and offshore wind farms", Environ Res Lett. 2017; 12:034022.

[2] H.M. Slot, ER. Gelinck, C. Rentrop, E. Van Der Heide, "Leading edge erosion of coated wind turbine blades: review of coating life models", Renew Energy 2015; 80:837–48.

[3] G. Marsh, "The challenge of wind turbine blade repair", Renewable Energy Focus, 12(4):62-6, 2011.

[4] Sandia National Lab News, Scan it and fix it with tech, JUN, 2019. sandia.gov/news/publications/labnews/articles/2019/0621/wind_turbines.html

[5] www.roperobotics.com

[6] S. Bernardini, F. Jovan, Z. Jiang, S. Watson, A. Weightman, P. Moradi, T. Richardson, R. Sadeghian, S. Sareh, "A Multi-Robot Platform for the Autonomous Operation and Maintenance of Offshore Wind Farms", AAMAS 2020, pp 1696-1700.

[7] S. Hawkins, and A. Nyboe, TEKNOBLADE REPAIR 9000 –a practical approach to Leading Edge Protection for wind turbine blades, 2019. https://my.eventbuizz.com/assets/editorImages/1570623644-Workshop_2_1400-_1515_-_Steffen_Hawkins.pdf

[8] Y. Su, M. Ahmadi, C. Bartneck, F. Steinicke, X. Chen, "Development of an Optical Tracking Based Teleoperation System with Virtual Reality", In 2019 14th IEEE Conference on Industrial Electronics and Applications (ICIEA) 2019 Jun 19 (pp. 1606-1611). IEEE.

[9] A. Patil, "Analysis of the inverse kinematics for 5 DOF robot arm using DH parameters", RCAR 2017, pp. 688-693.

[10] Z. Chen., H. Wang, X. Lu, Q. Pu, M. Li, and J. Yan, "Kinematics analysis and application of 5-DOF manipulator with special joint", 2017 Chinese Automation Congress, pp. 7421-7426.

[11] V. Kumar, S. Sen, SS. Roy, C. Har, SN. Shome, "Design optimization of serial link redundant manipulator: an approach using global performance metric", Procedia Technology. 2014 Jan 1; 14:43-50.

[12] S. Sareh, Y. Noh, T. Ranzani, H. Wurdemann, H. Liu and K. Althoefer, "A 7.5mm Steiner chain fibre-optic system for multi-segment flex sensing," *2015 IEEE/RSJ International Conference on Intelligent Robots and Systems (IROS)*, Hamburg, Germany, 2015, pp. 2336-2341, doi: 10.1109/IROS.2015.7353692.

[13] C. Chen, H.X. Li, H. Ding, Modeling and control of time-pressure dispensing for semiconductor manufacturing. Int J Automat Comput 4, 422–427 (2007).

[14] R. Sadeghian, M.T. Masoule, "An experimental study on the PID and Fuzzy-PID controllers on a designed two-wheeled self-balancing autonomous robot", In 2016 4th International Conference on Control, Instrumentation, and Automation (ICCIA) 2016 Jan 27 (pp. 313-318). IEEE.